ANL/APS/LS-269

Dose Measurements of Bremsstrahlung-Produced Neutrons at the Advanced Photon Source

M. Pisharody, E. Semones and P.K. Job
EXPERIMENTAL FACILITIES DIVISION
ADVANCED PHOTON SOURCE

ARGONNE NATIONAL LABORATORY
9700 S. Cass Ave., Argonne, IL-60439

August 1998

Acknowledgements

The authors are grateful to the members of the APS Collaborative Access Teams (CATs) belonging to Sector 11 (BESSRC CAT) and Sector 6 (μCAT) for providing their ID beamlines in order to conduct these experiments.

This work is supported by U.S. Department of Energy, BES-Material Sciences, under contract no. W-31-109-ENG-38.

Summary

Bremsstrahlung is generated in the storage rings of the synchrotron radiation facilities by the radiative interaction of the circulating particle beam with both the residual gas molecules and storage ring components. These bremsstrahlung photons, having an energy range of zero to the maximum energy of the particle beam, interact with beamline components like beam stops and collimators generating photoneutrons of varying energies. There are three main processes by which photoneutrons may be produced by the high energy bremsstrahlung photons: giant nuclear dipole resonance and decay (10 MeV $< E_\gamma <$ 30 MeV), quasi-deuteron production and decay (50 MeV $< E_\gamma <$ 300 MeV), and intranuclear cascade and evaporation ($E_\gamma >$ 140 MeV). The giant resonance neutrons are emitted almost isotropically and have an average energy of about 2 MeV. High energy neutrons (E > 10 MeV) emitted from the quasi-deuteron decay and intranuclear cascade are peaked in the forward direction. At the Advanced Photon Source (APS), where bremsstrahlung energy can be as high as 7 GeV, production of photoneutrons in varying yields is possible from all of the above three processes.

The bremsstrahlung produced along a typical 15.38-m straight path of the insertion device (ID) beamline of the APS has been measured and analyzed in previous studies. High-Z materials constituting the beamline components, such as collimators and beam stops, can produce photoneutrons upon interaction with these bremsstrahlung photons. The 1/E nature of the bremsstrahlung spectrum and the fact that the photoneutron production cross section is comparatively larger in the energy region 10 MeV $< E_\gamma <$ 30 MeV, results in the giant resonance interaction being the dominant mechanism that generates photoneutrons at the APS. Such neutron flux in the vicinities of the first optics

enclosures (FOEs) of ID beamlines is important, from the point of view of radiation protection of the personnel. Only a few of such neutron flux measurements were conducted at high photon energies. Monte Carlo codes and analytical formulas are used to calculate the differential photon track length in targets. Together with the known photoneutron cross sections, the neutron yields are then determined as a function of incident electron energy. Neutron fluence calculated from these yields assumes isotropic emission of neutrons from a point source target. Because neutron transport is not handled in most of these studies, possible neutron interactions inside the target are not accounted for in calculating the energy and intensity outside the target. There is also the uncertainty of photoneutron production cross section at higher energies.

A simultaneous measurement of bremsstrahlung and corresponding photoneutron production will provide photoneutron dose rates as a function of bremsstrahlung energy or power. Along with our already existing bremsstrahlung spectrum measurement expertise, we conducted simultaneous photoneutron dose measurements at the APS from thick targets of Fe, Cu, W, and Pb that are placed in the bremsstrahlung beam inside the FOE of the insertion device beamlines. An Andersson-Braun (AB) remmeter that houses a BF_3 detector, as well as a very sensitive pressurized ^{3}He detector, is used for neutron dose measurements. The dose equivalent rates, normalized to bremsstrahlung power, beam current, and storage ring vacuum, are measured for various targets.

This report details the experimental setup, data acquisition system, calibration procedures, analysis of the data and the results of the measurements.

Contents

List of Tables

List of Figures

Chapter 1

Introduction

1.1 Photonuclear Interactions

Photonuclear interactions [1, 2], also known as nuclear photo effect, are interactions in which a quantum of electromagnetic radiation disturbs the internal co ordinates of the nucleus. For photons having energies above typical binding energy range of the nuclei (>5 - 15 MeV), photonuclear interaction generally leads to emission of nucleons - photoneutrons as well as photoprotons. This nucleon emission is mainly due to three processes: giant nuclear dipole resonance, quasi-deuteron production and decay, and intranuclear cascade generated via photopion production.

1.1.1 Giant Nuclear Dipole Resonance

At incident photon energies between 10 - 30 MeV, photoabsorption leads to relative displacement of tightly bound neutrons and protons inside the nucleus. The struck nucleus may thus acquire an induced high frequency electric dipole moment. This dipole interaction causes an enhancement, known as the giant resonance, in the smooth continuous region of the nuclear absorption cross section. The integrated cross section for this process has been approximated using classical dipole sum rule modified for photonuclear interactions, and is given by [3, 4]:

$$\int \sigma(E_\gamma)dE_\gamma = \frac{2\pi^2 e^2 \hbar}{M_c} . \frac{NZ}{A}(1 + 0.8x), \tag{1}$$

where e is the electron charge, $\hbar$ is the Plank's constant divided by 2π (MeV-s), M is the mean nucleon mass (Mc^2 = 938.926 MeV), c is the speed of light ($cm\ s^{-1}$), N the neutron number, Z the proton number, $A = N + Z$, x is the fraction of attractive exchange force, and the coefficient 0.8 depends on the nuclear model that is used. The integral is extended right up to the pion threshold near 140 MeV. The energy at which the maximum in the giant resonance occurs varies with A. For light nuclei ($A < 30$), the maximum in the resonance occurs near 20 MeV, whereas for medium and heavy nuclei ($30 < A < 100$), it lies between 14 to 18 MeV. For $A \geq 120$, the energy of the maximum varies inversely as $A^{-1/3}$.

For heavy nuclei, the giant resonance decays mainly by neutron emission, (γ,n). Some contribution from double neutron emission, (γ,2n), is also possible for higher photon energies. Because of the presence of the large Coulomb barrier ($B \simeq Z^2 A^{-1/3}$ MeV) that lies well above the giant resonance energy in these nuclei, proton emission (γ,p) is strongly suppressed. For light nuclei, the giant resonance decay is predominantly by single nucleon emission - (γ,n) or (γ,p), with almost equal probability because of a compensation of the reduced Coulomb barrier by a slightly higher neutron separation energy - the binding energy of the last neutron added to the nucleus.

The giant resonance neutrons are of low energy (a few MeV), and the maximum cross section for their production is 1 - 2 mb/nucleon. As yet, no comprehensive data exists on the angular distribution of photoneutrons in general. The giant resonance neutrons consist of predominantly slow evaporation neutrons at low energies ($\leq$ 2.5 MeV) and a small fraction of fast direct neutrons, which dominate at higher energies. The evaporation neutrons are assumed to be isotropic and the direct neutrons anisotropic in emission [5]. Thus the giant resonance neutrons have an angular distribution that is symmetric about 90^o or even isotropic, irrespective of whether they originate from evaporation or direct production. Previous experimental measurements using 6.3 GeV bremsstrahlung on copper [6] yielded an isotropic distribution of emitted low energy neutrons in one detection method. The same measurement using another detection method showed a small forward maximum, with 60% of all the low energy neutrons between 0^o and 90^o.

For all practical purposes however, the angular distribution of photoneutrons is assumed to be largely isotropic at photon energies below 50 MeV.

1.1.2 Quasi-Deuteron Decay

At incident photon energies > 30 MeV, the cross sections for giant resonance neutron production decrease rapidly. Above 50 MeV, the predominant nuclear photoabsorption mechanism is through the quasi-deuteron effect [7]. Here, a nuclear model intermediate between the compound nucleus model and the independent nucleon model is assumed. Neutron-proton pairs inside the nucleus are considered as nuclear deuterons, and their wave function is taken as a multiple of the wave function of a free deuteron with the neutron and proton very close together. The remaining (A-2) nucleons constitute a potential well in which these quasi-deuterons move. The incident photon couples directly to the electric dipole moment of a quasi-deuteron in the nucleus causing photodisintegration (γ,np) of the deuteron. Assuming no further interactions in the nucleus (in light nuclei), the proton-neutron pair emerges with the energy and angular correlation appropriate to the deuteron photodisintegration. In heavy nuclei, such a correlation can not be observed as the proton and neutron emitted may undergo further interactions inside the nucleus. It is interesting to note that quasi-deuterons in the nucleus are not bound by the 2.2 MeV binding energy as in the case of a free deuteron. Instead, the proton and neutron of a quasi-deuteron possess positive energy due to their confinement in the nucleus, which enhances the high momentum components in the wave function. The average positive energy per nucleon constituting the quasi-deuteron is taken usually as 12 MeV [7]. Thus, a photon otherwise having insufficient momentum to eject high energy particles from the nucleus can do so by coupling to the dipole moment of the proton-neutron pair in the nucleus.

The cross section for the quasi-deuteron reaction, for photon energies above 100 MeV, has been estimated as [7]:

$$\sigma(\gamma, np) = L(\frac{NZ}{A})\sigma_d, \qquad (2)$$

where N and Z are the numbers of neutrons and protons in the nucleus, respectively, A is the atomic mass number of the nucleus, and σ_d is the known cross section for the free deuteron photodisintegration process [6]. L is the quasi-deuteron constant which is given as 6.4 by Levinger [7], though measurements [6, 8] to determine this value produced contradictory results. At lower photon energies (< 100 MeV), Equation 2 is expected to overestimate the nuclear cross section. Above 300 MeV, the quasi-deuteron cross section falls off approximately as the third power of the photon energy. Thus, this interaction may be considered insignificant beyond 500 MeV.

Moderately high energy neutrons and protons are emitted from the photodisintegration of the quasi-deuteron. The angular distribution features of the emitted protons and neutrons from quasi-deuteron decays are in general similar to those from the free deuteron photodisintegration. The neutron distribution is found to be only moderately forward peaked.

1.1.3 Intranuclear Cascade and Evaporation

Photoproduction of pions (photopions) becomes dominant for incident photon energies above 140 MeV - the mesonic threshold. In this mesonic region, the primary interaction is expected to be between the photon and a single nucleon since the wavelength of the photon is comparable to the diameter of a free nucleon. This interaction results in the production of one or more real π-mesons or pions. In fact, the nuclear absorption cross section above 140 MeV goes through a number of resonance peaks corresponding to single pion, dipion, tripion, etc., photoproduction thresholds. From nuclear emulsion studies [9], it has been shown that in complex nuclei about 80% of the photoproduced pions are reabsorbed in the same nucleus leading to the development of an intranuclear cascade followed by an evaporation process. The reabsorption or capture of the photopion that initiated the intranuclear cascade is assumed to occur through a few mechanisms [10]. These include pion capture by isobars (excited nucleons) that exist inside the nucleus or by quasi-deuterons inside the nucleus. Whatever may be the capture or reabsorption mechanism, high energy neutrons, as well as protons and pions, are emitted from the intranuclear cascade process. After the cascade, kinetic energies of the nucleons that did not escape from the nucleus get shared among all nucleons, and the excited nucleus subsequently evaporates[1] emitting low energy neutrons, protons, and even photons.

The high energy particles emitted during an intranuclear cascade process are most likely to be peaked in the forward direction because of the large center of mass motion for the absorption of high energy photons. During the subsequent evaporation of the nucleus, however, isotropic emission is expected for the lower energy particles. Charged particles that are emitted toward the end of the evaporation process are subjected to a smaller Coulomb barrier than those emitted initially because of the loss of charges from the initial nucleus. Thus, emission of heavier charged particles, such as alphas and deuterons, is possible toward the end of a long evaporation cascade (high initial excitation of the nucleus). The cross sections for photoneutron production in the high energy domain are not very well known. Based on nuclear emulsion measurements [11, 9] and Monte Carlo calculations for nuclear evaporation [16], approximate relations for the production cross section of neutrons and protons, both having energies above 25 MeV, are available for photons of energy > 250 MeV [6].

Of all the three photonuclear interaction theories discussed, only the lower energy giant resonance dipole region is well understood. However, calculations that make use of the quasi-deuteron model and intranuclear cascade model (for single pion production) have been shown to yield over-all agreement with various types of photonuclear experimental data for a wide range in atomic mass numbers ($A > 12$) and over a wide range in photon energies ($40 < E_\gamma < 350 MeV$) [17].

1.2 Photoneutrons from Electron Storage Rings

With the advent of high energy electron accelerators, photoneutron yields at higher photon energies have become important. The source of high energy photons in an electron storage ring is bremsstrahlung that is generated when the circulating electron or positron beam interacts with the residual gas molecules in the vacuum or the storage

[1]Such an evaporation process results in the formation of "photostars" - multiprong events in nuclear emulsions that represent production of two or more charged particles through photodisintegration. It has been observed that the number of multiprong photostars rises very sharply above the mesonic threshold [9, 11, 12, 13]. Monte Carlo calculations of intranuclear cascades [14, 15] have shown good agreement with the above mentioned experimental data.

ring components. The bremsstrahlung spectrum is approximately $\frac{1}{E_\gamma}$ in nature with a maximum energy equal to the energy of the circulating beam in the storage ring. The bremsstrahlung produced along typical 15.38-m straight sections of the insertion device (ID) beamlines of the Advanced Photon Source (APS) has been measured in previous studies [18, 19]. Bremsstrahlung produced from the storage ring interacts with the high-Z materials in the beamline, such as beam stops and collimators, to generate photoneutrons by any or all processes detailed above.

1.2.1 Monte Carlo Tools

Except for the giant resonance cross sections [20, 21], other photonuclear interaction cross sections at high energies are not readily available. As discussed earlier, these are to be calculated from appropriate nuclear models. The photonuclear interaction Monte Carlo PICA (Photon-Induced Intranuclear Cascade Analysis) [22] calculates the results of nuclear reactions caused by the collision of medium energy photons ($30 < E_\gamma < 1000$ MeV) with the nuclei [17]. PICA also calculates results of giant resonance dipole interactions using available cross sections [20, 21]. PICA can accommodate both incident monoenergetic photons as well as incident bremsstrahlung photon spectra. The medium energy interaction cross sections are derived from the quasi-deuteron model [7]. The secondary interaction processes, such as pion absorption and nucleon-nucleus interactions that follow the photon absorption, are calculated using the intranuclear cascade concept [23, 24]. The de-excitation of the compound nucleus following the cascade phase is handled by an evaporation model [25, 16, 26]. Each particle involved in a collision is traced through the nucleus using appropriate particle-particle cross sections, detailed earlier, until the particle escapes or is recaptured by the nucleus. Fermi momentum of the struck particle, the Pauli exclusion principle, and the nonuniform nucleon density distribution are taken into account in all parts of the calculation. Calculations from PICA show that, in general, photoneutron spectra from the bremsstrahlung are dominated by the giant resonance component ($\geq 70\%$). This is because of the $\frac{1}{E_\gamma}$ nature of the bremsstrahlung together with the comparatively higher cross sections for photoneutrons in the $10 < E_\gamma < 30$ MeV region (giant resonance region). A general purpose code MCNP (Monte Carlo N-Particle) [27] also accounts for photoneutron production in photon collision events. Here, the photoneutron cross sections have to be user supplied into the MCNP cross-section data structure.

1.2.2 Previous Measurements

Giant resonance neutron yields and doses have been studied in previous measurements mainly using incident electrons [28, 29, 30]. For a thick target, the incident electron beam generates a shower that contains electrons and photons of lesser energy. The low energy photons in the shower produce giant resonance neutrons, while the direct interaction of the shower electrons with the nucleus is α (fine structure constant) times weaker than its photonuclear counterpart and can be neglected. Thin targets will yield approximately equal contributions from electronuclear and photonuclear processes, and a separation of these effects has to be performed. Neutron yield per incident electron, having energies in the range 10 to 36 MeV, from various target materials ranging in thickness from one to several radiation lengths have been determined in earlier measurements [28]. There also has been an experimental study [31] that involves photoneutron dose rates from gas bremsstrahlung striking beamline components in a 3 GeV electron storage ring. In this experiment, giant resonance neutron dose rates around an undulator beamline were measured and compared with the predictions of the EGS4 [32] Monte Carlo code. The dose rates resulting from photoneutrons generated by the gas bremsstrahlung striking two different beamline components (copper slits and tungsten beamstops), as measured by a moderated BF_3 detector positioned laterally in relation to the targets, were normalized to source parameters such as, the circulating beam energy and current and the average vacuum pressure in the long straight section of the undulator beamline.

Analytical formulas have been used in calculating yields of low energy photoneutrons released by electrons up to 1 GeV incident on semi-infinite targets of various materials [29]. These yields are based on photon differential track-length distributions in the material and the available photoneutron cross sections [20, 33] that explicitly take into account the neutron multiplicity - $(\gamma, n), (\gamma, 2n), (\gamma, 3n)$, etc. In another study [30], EGS4 was utilized to estimate the differential photon track length in thick targets. The giant resonance neutron yields are then evaluated by integrating the product of the differential photon track length and the published giant resonance neutron cross sections, over the photon energy spectra generated by electrons with energies from 18 MeV to 10 GeV. For thin targets, both the bremsstrahlung photon as well as virtual photon differential track lengths were calculated using already developed analytical formulas [34] based on Weizsacker-Williams method. The EGS4 study is then validated by an experimental measurement of giant resonance neutron yield produced by 34 MeV electrons. A scaling function had been determined to estimate the neutron yields from thin targets, given the thick target formula. Recently a study of the production as well as transport of the giant resonance neutrons, with regard to their spectral and angular distributions, has been conducted [35] by making use of a coupling procedure between EGS4 and MORSE [36] Monte Carlo codes. This study makes a distinction between the spectral and angular distributions of the directly produced and evaporation-produced giant resonance photoneutrons from incident photons of energies < 30 MeV.

1.2.3 Photoneutron Production at the APS

In the present experiment at APS, simultaneous measurements of bremsstrahlung and corresponding photoneutron production from thick Fe, Cu, W, and Pb targets have been conducted at 7 GeV positron beam energy. From these measurements, the photoneutron dose equivalent rate as a function of the bremsstrahlung energy or power radiated are determined. The experiment has been conducted in the first optics enclosures (FOEs) of undulator insertion device (ID) beamlines 11-ID and 6-ID of the APS. The ID is kept fully open in order to minimize the synchrotron radiation background. The bremsstrahlung in the FOE is measured by means of a sensitive electromagnetic calorimeter, details of which can be found in earlier publications [18, 19]. Photoneutrons are generated from four target materials - Fe, Cu, W, and Pb, each of which is approximately 20 radiation lengths long and 6 Moliere radii wide. The dimensions of these targets have been chosen to maximize the shower containment and minimize the self absorption of generated neutrons. Targets are placed in the bremsstrahlung beam inside the FOE following a bremsstrahlung measurement, and the photoneutron dose rates are measured at 80 cm perpendicular to the beam direction using the Andersson-Braun (AB) remmeter [37]. This is followed by another bremsstrahlung measurement. Data are acquired for various beam currents, and the vacuum and residual gas composition are documented.

Chapter 2

The Experimental Setup and Data Acquisition System

2.1 Bremsstrahlung Measurements

Bremsstrahlung energy spectra from ID beamlines at the APS have been measured by a fast and sensitive electromagnetic calorimeter made of 25 lead-glass detectors, each 6.3 cm $\times$ 6.3 cm $\times$ 35 cm, stacked into a 5 $\times$ 5 array [18, 19]. The energy resolution of this detector is about $(7\pm2)\%/\sqrt{E_\gamma}$ and the response time is typically about 20 nsec. The bremsstrahlung beam is aligned along the central lead-glass detector. The central 3 $\times$ 3 detector matrix of the calorimeter has been found to contain 100% of the electromagnetic shower in the lateral direction and approximately 96% in the longitudinal direction. Energies of the incident bremsstrahlung photons are measured on an event-per-event basis. Individual lead-glass detector signals are read through photomultiplier tubes; the signals are then fed into fast encoding and read out ADCs (FERA). The signal from the central lead-glass detector is split to a trigger circuit that is used to generate a gate to the ADCs upon real energy deposition. Digitized data from the ADCs are stored into a 16K memory unit for subsequent slow read out by a computer. A schematic of the calorimeter and associated data acquisition system is shown in Figure 1.

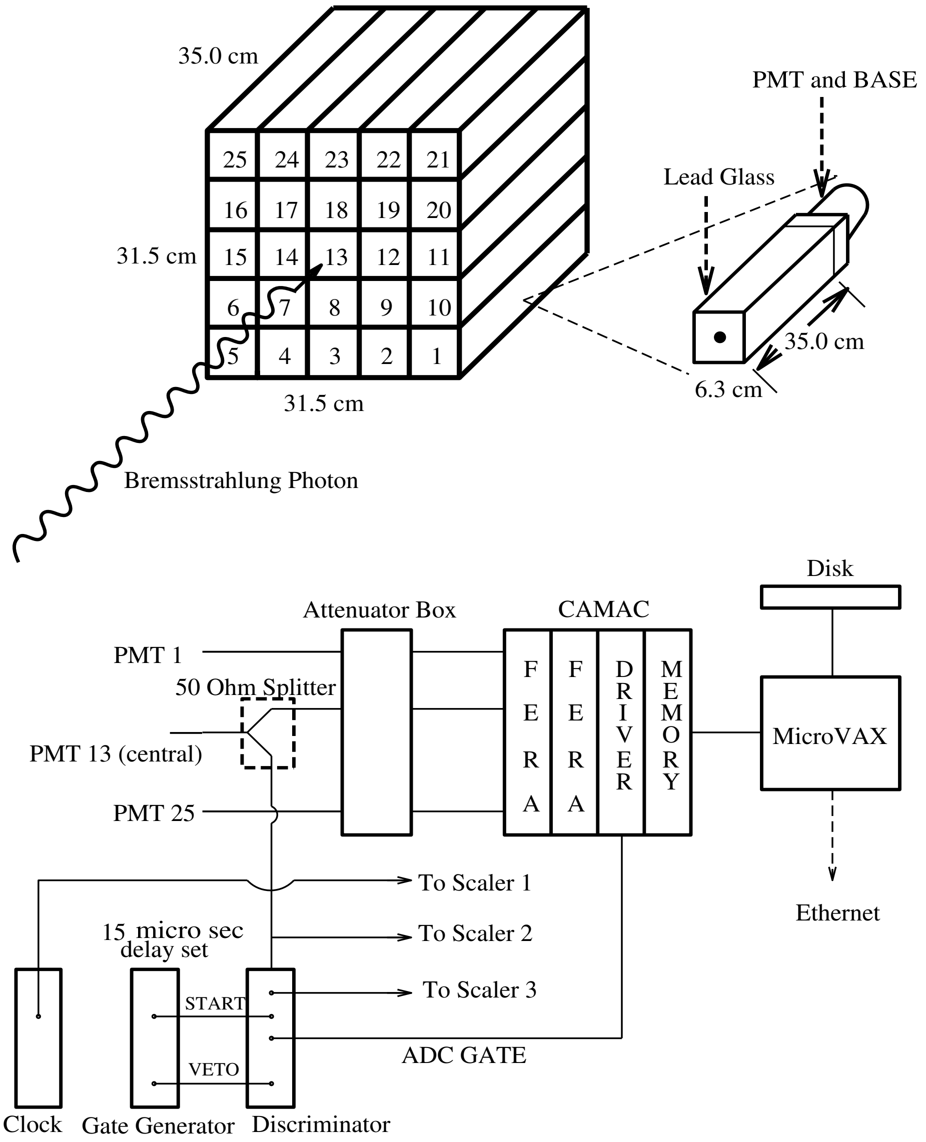

Figure 1: The lead-glass electromagnetic calorimeter and associated data acquisition system that are used to measure the bremsstrahlung spectrum and power.

2.2 Photoneutron Measurements

The dose equivalent, which is the quantity used as the measure of the radiobiological hazard associated with a given radiation field in radiation protection purposes, is a strong function of the neutron energy spectrum and fluence of the corresponding field. It has been found that a class of instruments known as remmeters have the capability to estimate integral neutron dose equivalent without having to know either the neutron energy spectrum or the neutron fluence. An artificial neutron sensitivity is given to remmeters such that the response to a neutron fluence as a function of neutron energy varies in accordance with the maximum dose equivalent that would be created in a human body exposed to that fluence. Remmeters, designed to have such an approximate correct dose response over a neutron energy range of thermal to $\sim$ 15 MeV, when used to detect neutrons from a polyenergetic spectrum will automatically fold in proper weighting factors for neutrons in this energy range and provide an appropriate measure of the corresponding dose for radiation protection purposes.

The average energy of photoneutrons emitted in the giant resonance photonuclear process is estimated to be about 2 MeV. Thus, photoneutrons in general fall in the medium-to-fast neutron category. The Andersson-Braun (AB) remmeter has been generally used for neutron dose measurements independently of incident neutron energies from thermal to 15 MeV. It consists of a proportional tube surrounded by cylindrical shields made of polyethylene and boron plastic that provide the appropriate amount of neutron moderation and absorption in order to obtain an approximately correct dose response. Circular disks of the same materials and thicknesses make up the ends of the cylindrical moderator. A BF_3 or a highly sensitive ^{3}He proportional tube can generally be used along with the AB shell. The detector pulse height spectrum itself does not contain any information about the incident neutron energy. It is a function only of the size and geometry of the detector. Gamma rays, which often accompany the neutron field that is being measured, primarily interact with the wall of the counter generating electrons that may produce ionization of the proportional gas. Most of these undesired interactions will result in low-amplitude pulses because of the low stopping power for electrons in gases. In the pulse height spectrum, these events will translate into a very well separable tail, which can be eliminated by simple amplitude discrimination without

Table 1: Target dimensions and elemental purities.

Target Material	Length	Width	Elemental Purity
Fe	21.9 X_0 (38.4 cm)	5.9 X_m (9.6 cm)	93% Fe
Cu	19.5 X_0 (28.0 cm)	6.2 X_m (8.8 cm)	93% Cu
W	21.3 X_0 (8.0 cm)	6.1 X_m (6.0 cm)	95% W
Pb	20.5 X_0 (11.6 cm)	5.6 X_m (9.0 cm)	99% Pb

affecting neutron detection efficiency.

2.2.1 Experimental Setup

A standard Andersson-Braun (AB) remmeter, which utilizes a N. Wood G-10-2A BF_3 tube (60 mm Hg) and an LND 252167 ^{3}He (270 mm of Hg) tube, are used along with the associated data acquisition system for the photoneutron detection and dose measurement. The signal from the proportional tube is fed into a amplifier-multichannel analyzer (MCA) unit through a preamplifier. The pulse height spectrum from the MCA is then written onto a PC.

Four targets - Fe, Cu, W, and Pb, each approximately 20 radiation lengths (X_0) long and 6 Moliere radii (X_m) in the lateral dimension - are used for these measurements. The dimensions of the targets have been chosen such that approximately 99% of the electromagnetic shower in both the longitudinal and the transverse directions are contained within the target. The selection of the typical lateral dimension of the targets is also to minimize self-absorption of generated giant resonance photoneutrons within the target. Only a 6% reduction in neutron fluence is estimated at these target dimensions [38]. A complete description of the four targets used is summarized in Table 1. The impurities present in the targets (7% in Fe and Cu, 1% in Pb, and 5% in W) are traces of other metals having atomic numbers (Z) close to that of the target material. Thus, the resulting correction in Z is estimated to be less than 1%.

A schematic of the combined bremsstrahlung-photoneutron experimental setup is shown in Figure 2. The target is placed inside the FOE of the beamline at about 170 cm from the beam exit window, aligned lengthwise along the photon beam. The lead-glass electromagnetic calorimeter, the central tube of which is also aligned along the photon beam, is placed approximately 40 cm behind the target. During bremsstrahlung measurements, the target is removed from the photon beam. The neutron dose equivalent rate measurements are made perpendicular to the incident photon beam direction. The Andersson-Braun remmeter is placed at a distance of about 80 cm at right angles to the aligned target. The center of the Andersson-Braun remmeter is aligned with the center of each of the targets used. Signals from the lead-glass calorimeter are sent to the data acquisition system located outside the FOE [18, 19]. Pulses from the proportional tubes are fed into a charge-sensitive preamplifier placed inside the FOE. The output of the preamplifier is then taken out of the FOE to the amplifier and multichannel analyzer. The insertion device gap is kept in the full open position to minimize the low energy synchrotron radiation. A copper shield, which is about $0.5X_0$ in thickness, is also placed in front of the lead-glass calorimeter to screen against low energy residual synchrotron radiation arriving at the FOE. That the photon events detected by the proportional tube are indeed from the scattering of residual synchrotron radiation is confirmed by inspecting the pulse height spectra with and without a target in the bremsstrahlung beam path. The respective pulse height distributions were found to have photon signals similar in amplitudes indicating the source as scattered synchrotron radiation. The already inherent good separation of photon and neutron events in the pulse height distribution from both the BF_3 and ^{3}He tubes has been improved by the introduction of a thin Pb sleeve around the moderator without adversely affecting the neutron counts. The neutron attenuation as well as the high energy neutron enhancement effects due to the presence of this Pb sleeve are found to be minimal.

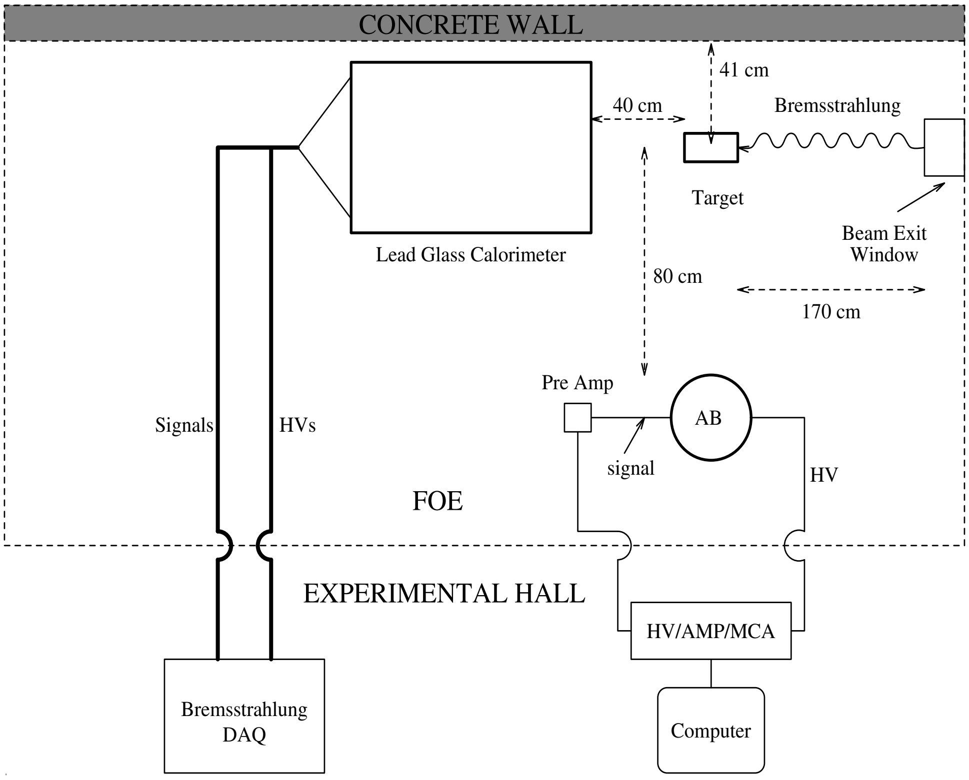

Figure 2: Schematic of the top view of the Andersson-Braun remmeter and the calorimeter along with the associated data acquisition systems that measure the photoneutron dose equivalent rates and the bremsstrahlung power.

Chapter 3

Experimental Procedure and Data Acquisition

3.1 Experimental Procedure

Experimental runs are conducted in such a way that each of the photoneutron measurement is preceded and followed by one bremsstrahlung measurement. Once bremsstrahlung data set is collected, the target is placed in its marked position along the photon beam and the corresponding photoneutron data set is acquired, upon completion of which another bremsstrahlung data set is taken by removing the target. The time elapsed between measurements is kept as minimal as possible. The average of the energy or power from the two bremsstrahlung data sets is then used to normalize the photoneutron data collected in between. The typical long particle beam lifetime in the storage ring kept changes in the beam current with respect to time to a minimum. Thus the measurements can be approximated as simultaneous. The straight section vacuum, as measured by six ion gauges, has been written into a data file at every two-minute interval [18, 19].

3.2 Data Acquisition

Details of the bremsstrahlung experimental and data acquisition procedures were described previously [18, 19]. As discussed earlier, both BF_3 and ^3He proportional tube AB remmeters have been used for the corresponding photoneutron dose measurements. Data are collected from all the four photoneutron targets using both the AB detectors.

3.2.1 Andersson-Braun Calibration

The Andersson-Braun remmeter was calibrated against an unmoderated Cf-252 source in order to convert the neutron count rates into corresponding dose equivalent rates. Both BF_3 as well as ^3He tubes were calibrated separately. During calibration, the AB is aligned and placed at a distance of 50 cm from the Cf-252 source when using BF_3 as the detector. For ^3He, the distance from the source is chosen as 75 cm [1]. The corresponding pulse height distributions from each of the tubes are shown in Figure 3. The sensitivities of the BF_3 tube and ^3He tubes used are then determined as 0.46 mrem/h/cps and 0.13 mrem/h/cps, respectively, to the bare Cf-252 source. The scattered neutron response at both these distances was determined to be less than 10%. The 2-mm-thick Pb sleeve that has been used to wrap around the AB outer moderator during the actual experimental run to reduce photon interactions was not used during the calibration procedure as its effects were found to be minimal.

3.2.2 Storage Ring Vacuum and Residual Gas Data

The intensity of the gas bremsstrahlung and hence that of the photoneutrons generated is a function of the stored beam current, atomic number of the residual gas, and the storage ring vacuum. Thus, during the experimental runs at both the insertion device beamlines, data have been collected in order to determine the correct values of the storage ring vacuum and the chemical composition of the residual gas inside the storage ring (details of this procedure can be found in previous publications [18, 19]). Storage ring vacuum determined as a function of the stored beam current is shown in Figure 4(A)

[1] ^3He tube being highly sensitive, generates significant dead time at 50 cm from the Cf-252 source.

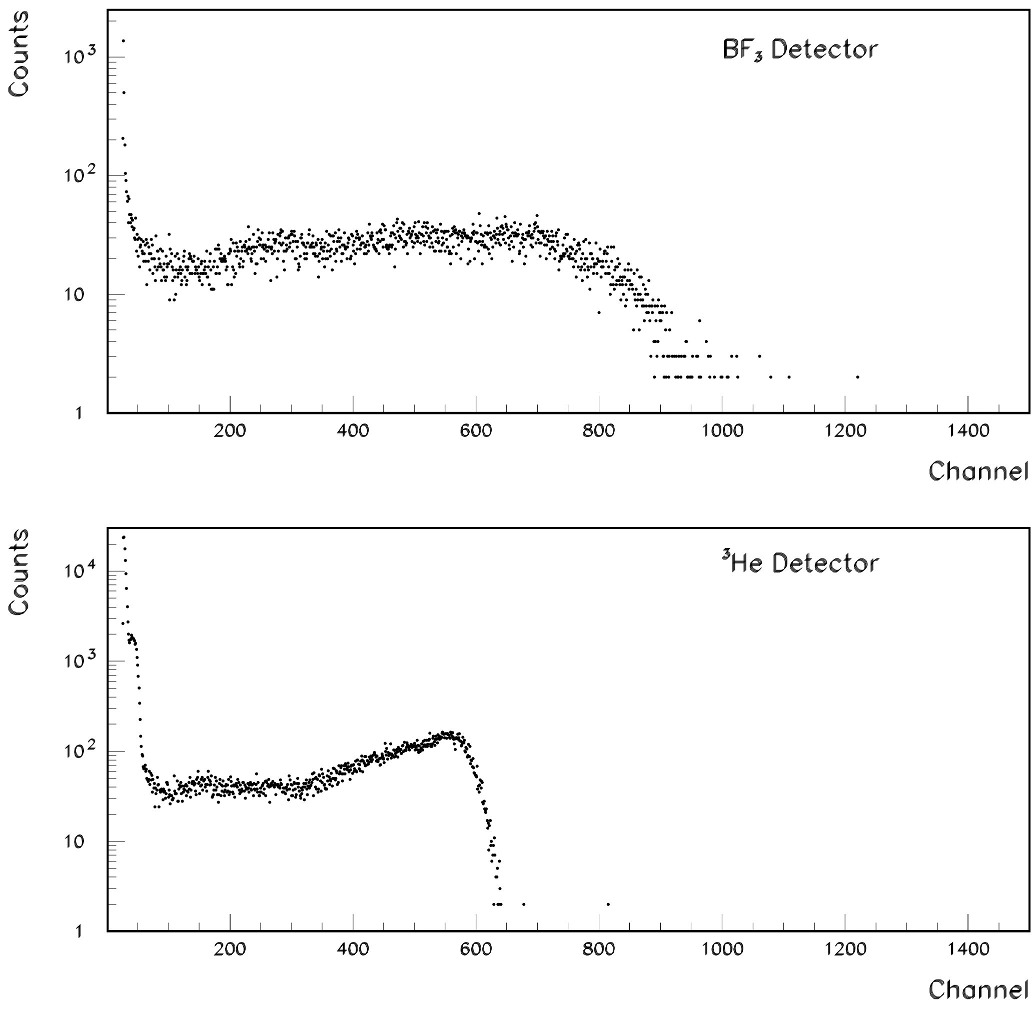

Figure 3: Pulse height distributions from the BF_3 and ^{3}He tubes used in the Andersson-Braun moderator during calibration with the Cf-252 source.

Table 2: Typical residual gas measurement results for 11-ID and for 6-ID at a given beam current.

Beamline	Mass Number	Residual Gas Component	Mole Fraction (%)	Weight Percent (%)
11-ID	2	H_2	80.0	25.9
	16	CH_4	4.5	11.7
	19	F	5.7	17.7
	28	N_2/CO	9.8	44.7
6-ID	2	H_2	57.4	8.3
	18	H_2O	13.1	17.0
	28	N_2/CO	16.4	33.1
	44	CO_2	13.1	41.6

and 4(B) for beamlines 11-ID and 6-ID, respectively. The vacuum can be seen varying linearly within the shown beam current range (50 mA to 100 mA) that was available during the measurement. Table 2 shows typical residual gas component information measured at 11-ID and 6-ID at a given beam current. Effective Z's for the gas composition at these beam currents can then be determined. For the results shown in Table 2, the effective Z has been calculated as 3.18 for 11-ID and 4.08 for 6-ID. Several such residual gas measurements have been conducted at various beam currents corresponding to experimental runs. At 6-ID, the RGA was conducted at the straight section. At 11-ID, RGA was not available from the straight section and hence was extracted from the front-end section - approximately 6 to 8 meters downstream of the insertion device. The residual gas composition at the straight section is obviously different from that of the front end.

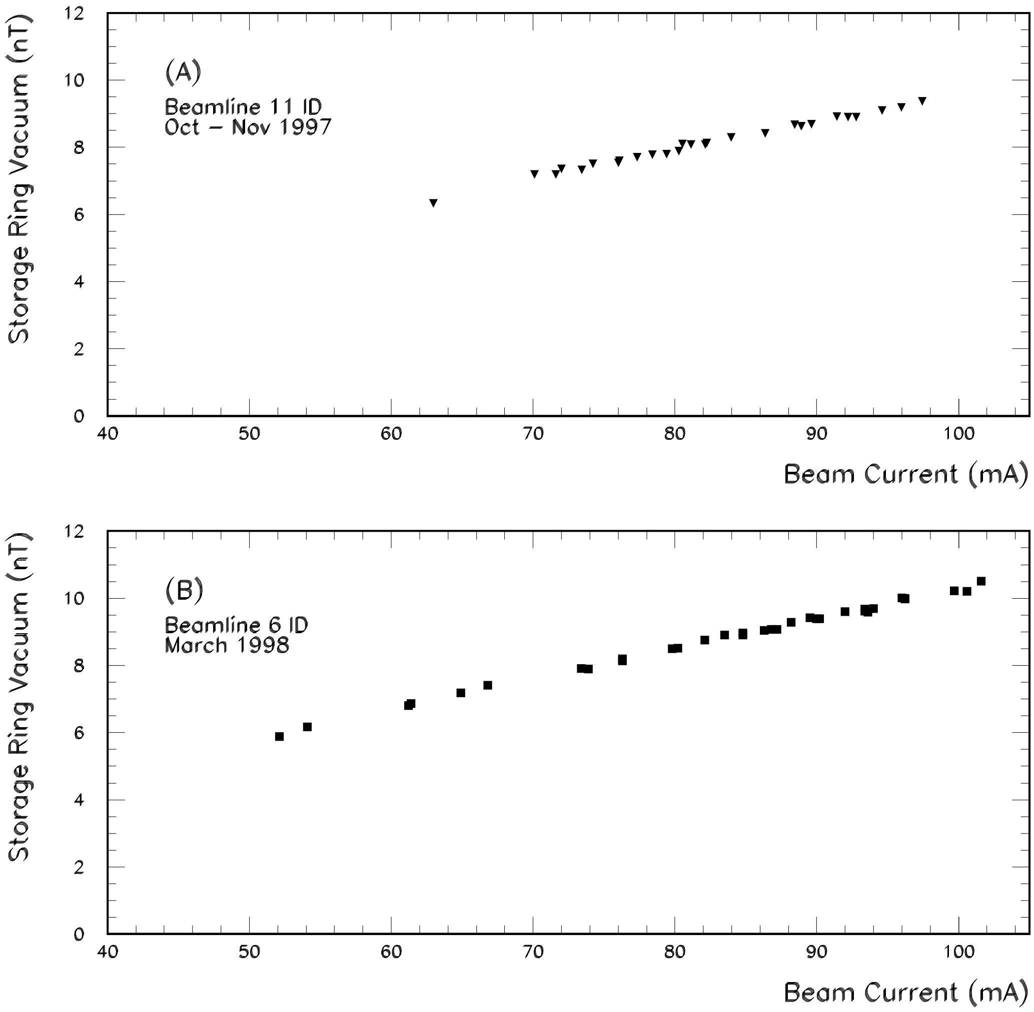

Figure 4: Variation of storage ring vacuum as a function of beam current at beamlines 11-ID and 6-ID.

Chapter 4

Results and Analysis

The data in this report come from two separate experimental runs: one conducted in October - November 1997 and the other in March 1998. The first run was conducted at ID beamline 11 and the latter at ID beamline 6. The vertical dimension of the vacuum chamber at 11-ID is 12 mm and that at 6-ID is 8 mm.

4.1 Bremsstrahlung Power

The calibration procedure of the lead-glass calorimeter, the nature of the raw ADC bremsstrahlung distributions, and various systematic errors involved have been discussed in detail previously [18, 19]. Figure 5 (A) and (B) show measured bremsstrahlung energy spectra, normalized to the storage ring vacuum, for a few typical beam currents of the two experimental runs. Systematic errors associated with the measurements, such as dead-time losses, longitudinal shower leakage, and low energy cut off, have been applied to the energy spectra in Figure 5 to obtain the corrected results shown in Tables 3 and 4. Results from Table 3 and Table 4 are also shown plotted in Figure 6 (A) and (B). Figure 6 (A) shows the variation of bremsstrahlung energy, normalized to the beam current, as a function of the storage ring vacuum, while (B) gives the variation of the former, normalized to both the vacuum and beam current, as a function of the beam current. The nonlinear nature of the points in Figure 6 (A) makes extrapolating the plot difficult, and hence separating the gas and non-gas bremsstrahlung components

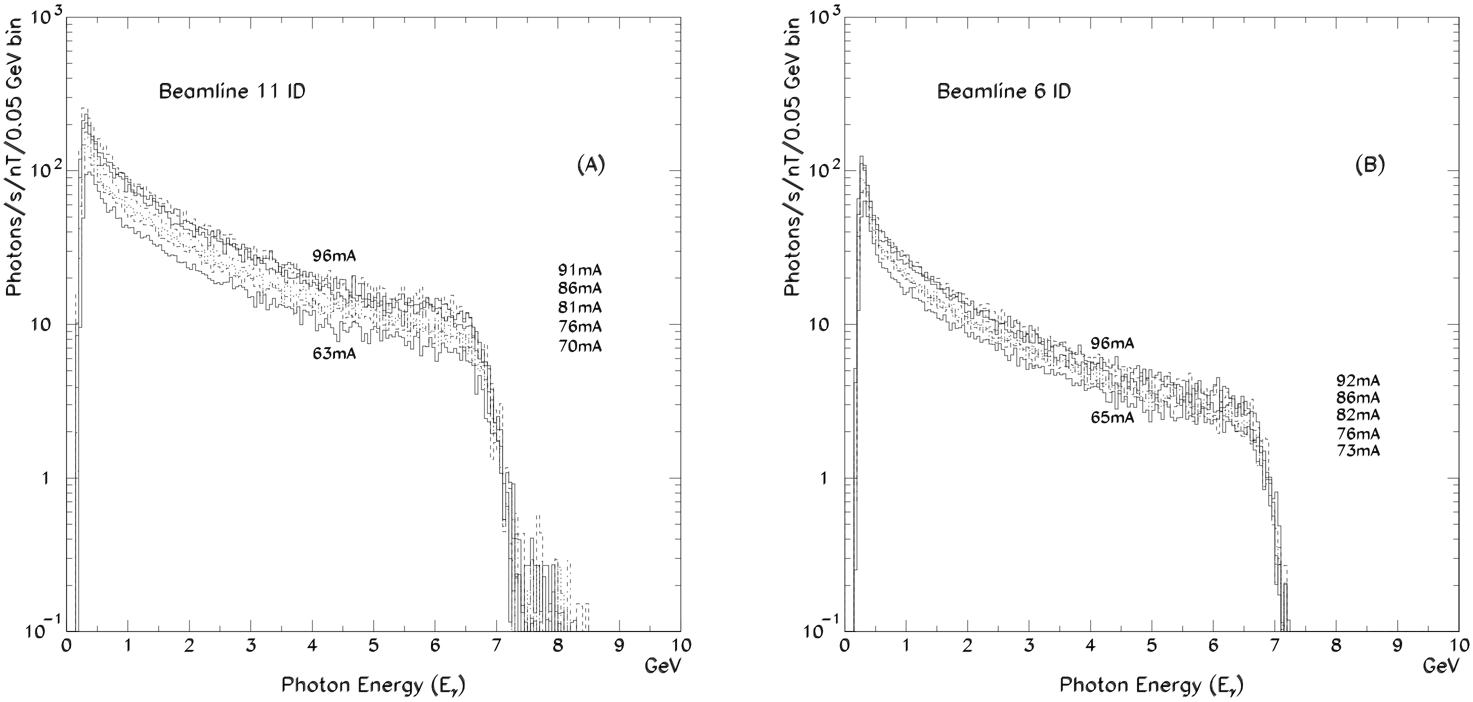

Figure 5: Bremsstrahlung energy spectra, corrected for dead-time losses, for typical beam currents during the two experimental runs at beamlines 11-ID (A) and 6-ID (B).

non-trivial [18, 19]. The bremsstrahlung contribution from each individual beamline is fairly constant as seen in Figure 6 (B) - an average of 118.0±9 GeV/s/nT/mA from 11-ID and 36±2 GeV/s/nT/mA from 6-ID. The difference in the contribution between the beamlines is due to the variations in vacuum and temperature (RF heating) profiles along the vacuum chamber, the variation in residual gas composition in the straight section, and also to the presence of non-gas bremsstrahlung in the straight section, generated by the interaction of the beam halo with storage ring components. The bremsstrahlung power in kilowatts, normalized to the storage ring vacuum, is also given in Figure 7 for the two beamlines as a function of the beam current. The statistical error spread on the data points is determined to be of the order of 10^{-11}. It is clear that the power varies linearly with the beam current. Average normalized bremsstrahlung powers of

Table 3: Bremsstrahlung power for various beam currents from the 15.38 m of positron beam straight path at beamline 11-ID. A 12% correction due to the threshold cut-off was determined in the photon count rate and has been incorporated in the bremsstrahlung photon rate.

Beam Current I_b (mA)	Estimated Vacuum P (nT)	Bremsstrahlung Photon Rate N_γ (/s/nT/mA)	Bremsstrahlung Energy Rate E_γ (GeV/s/nT/mA)
63.0	6.33	50.0±4	99.0±9
70.1	7.18	55.0±4	108.0±9
71.6	7.19	55.0±4	108.0±9
72.0	7.35	55.0±4	108.0±9
73.4	7.32	61.0±4	117.0±9
74.2	7.51	58.0±4	114.0±9
76.0	7.53	56.0±4	109.0±9
76.1	7.59	60.0±4	118.0±9
77.3	7.70	57.0±4	112.0±9
78.4	7.77	60.0±4	116.0±9
79.4	7.80	61.0±4	117.0±9
80.3	7.88	60.0±4	119.0±9
80.5	8.09	60.0±4	116.0±9
81.1	8.08	61.0±4	117.0±9
82.1	8.08	61.0±4	120.0±9
82.2	8.13	55.0±4	111.0±9
84.0	8.30	64.0±4	122.0±9
86.3	8.42	65.0±4	123.0±9
88.4	8.67	65.0±4	125.0±9
88.9	8.63	68.0±4	128.0±9
89.6	8.69	65.0±4	126.0±9
91.4	8.91	68.0±4	129.0±9
92.2	8.90	65.0±4	126.0±9
92.8	8.89	64.0±4	121.0±9
94.6	9.10	68.0±4	129.0±9
96.0	9.18	70.0±4	129.0±9
97.4	9.37	67.0±4	126.0±9

Table 4: Bremsstrahlung power for various beam currents from the 15.38 m of positron beam straight path at beamline 6-ID. A 12% correction due to the threshold cut-off was determined in the photon count rate and has been incorporated in the bremsstrahlung photon rate.

Beam Current I_b (mA)	Estimated Vacuum P (nT)	Bremsstrahlung Photon Rate N_γ (/s/nT/mA)	Bremsstrahlung Energy Rate E_γ (GeV/s/nT/mA)
52.1	5.89	21±1	35.0±2
54.1	6.18	19±1	33.0±2
61.2	6.80	21±1	35.0±2
61.4	6.86	19±1	34.0±2
64.9	7.18	19±1	34.0±2
66.8	7.41	21±1	35.0±2
73.4	7.91	20±1	35.0±2
73.9	7.89	19±1	34.0±2
76.3	8.13	21±1	35.0±2
76.3	8.20	21±1	35.0±2
79.8	8.50	20±1	35.0±2
80.2	8.52	21±1	36.0±2
82.1	8.76	19±1	35.0±2
83.5	8.90	20±1	36.0±2
84.8	8.97	22±1	36.0±2
84.8	8.91	22±1	37.0±2
86.3	9.04	22±1	37.0±2
86.8	9.06	22±1	37.0±2
87.2	9.07	20±1	36.0±2
88.2	9.28	22±1	36.0±2
89.5	9.42	22±1	36.0±2
90.0	9.39	22±1	37.0±2
90.2	9.34	22±1	37.0±2
92.0	9.60	23±1	38.0±2
93.4	9.68	22±1	37.0±2
93.4	9.62	22±1	37.0±2
93.6	9.59	20±1	36.0±2
94.0	9.70	22±1	37.0±2
96.0	10.01	22±1	37.0±2
96.2	9.99	21±1	37.0±2
96.2	9.98	20±1	36.0±2
99.7	10.21	22±1	37.0±2
100.6	10.21	19±1	33.0±2
101.6	10.51	20±1	35.0±2

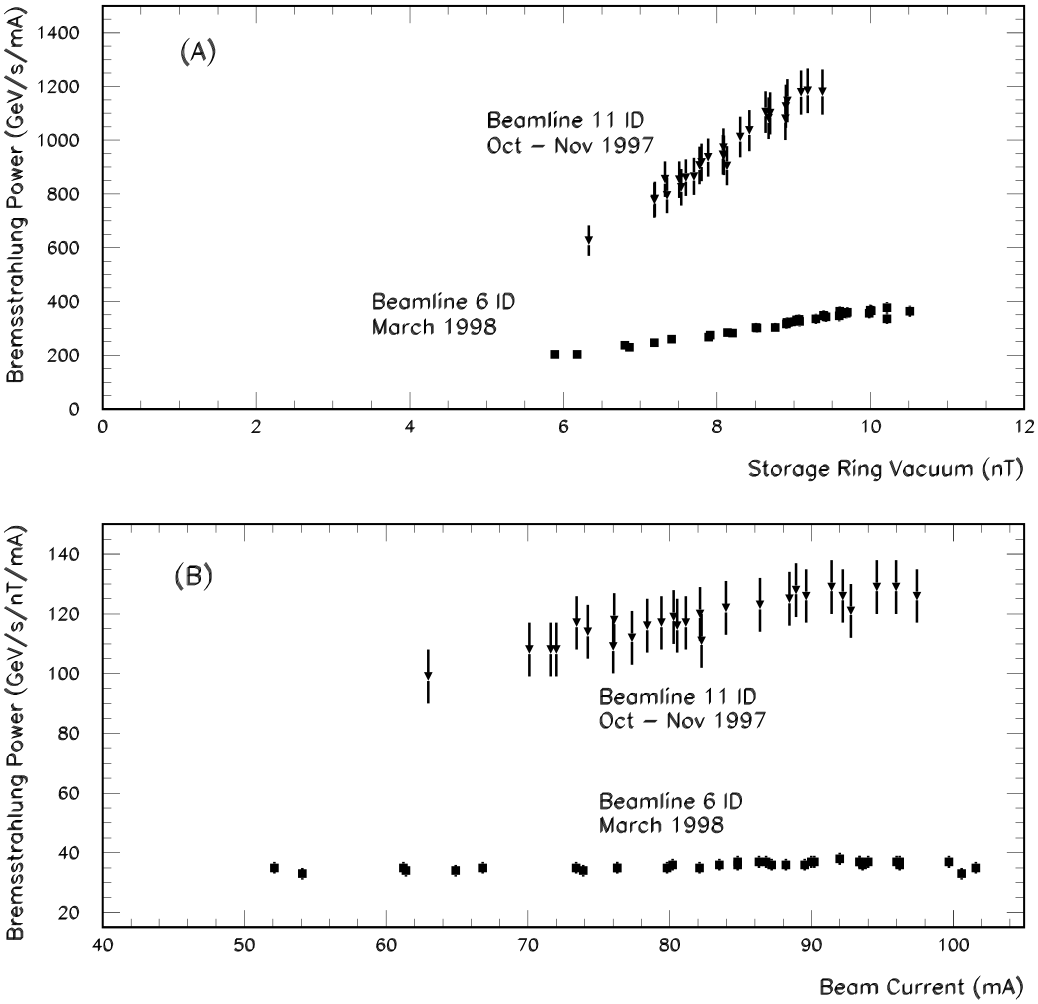

Figure 6: (A) Bremsstrahlung power, normalized to the beam current, as a function of the storage ring vacuum for the two experimental runs at beamlines 11-ID and 6-ID. (B) The slopes of the lines in (A), which give the normalized bremsstrahlung contribution from both beamlines, as a function of the beam current.

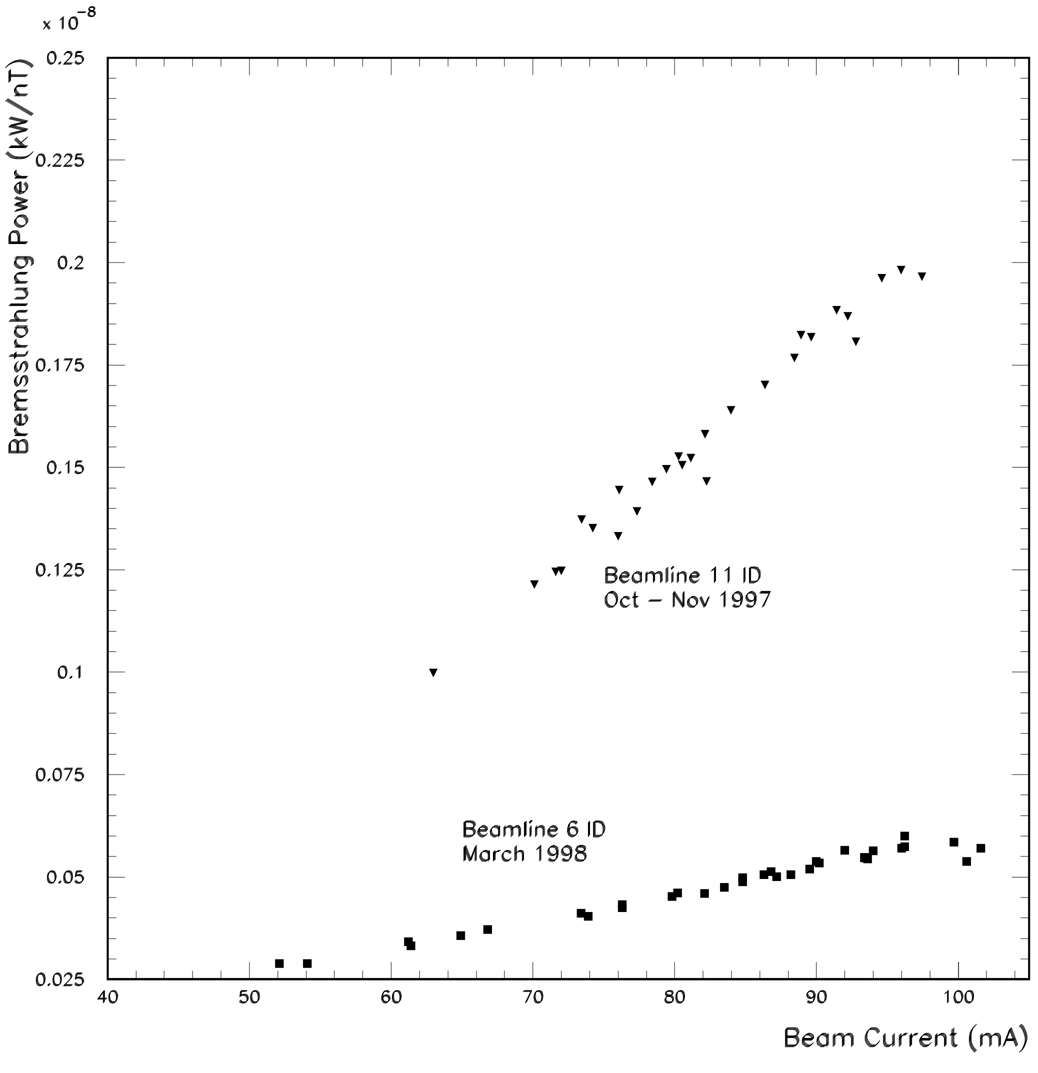

Figure 7: Bremsstrahlung power in kilowatts, normalized to the storage ring vacuum, as a function of the beam current for the two experimental runs at beamlines 11-ID and 6-ID.

$(2.0 \pm 0.14) \times 10^{-8}$ W/nT/mA and $(0.6 \pm 0.03) \times 10^{-8}$ W/nT/mA have been measured for beamline 11-ID and 6-ID, respectively.

The following conclusions can be made from the results of this section. Clearly, the bremsstrahlung varies with beam current and storage ring vacuum. The bremsstrahlung power, normalized both to the vacuum and beam current, is fairly constant within a beamline for a given storage ring fill pattern but may vary from beamline to beamline. The reasons for such a beamline to beamline variation of the normalized bremsstrahlung power are attributed to the variation of vacuum profile along the vacuum chamber, the variation of residual gas composition in the straight section, the variation of temperature profile along the vacuum chamber due to RF heating, and the presence of a non-gas bremsstrahlung component. The production of the non-gas bremsstrahlung depends upon the vacuum chamber dimensions, the relative position of the beam halo with respect to the vacuum chamber, and the maximum bunch current in the storage ring as determined by the storage ring fill pattern. Independent measurements from six beamlines at the APS (the present two measurements and four earlier measurements [18, 19]) have shown a variation in the normalized bremsstrahlung power, as much as a factor of ten, due to any or a combination of the above discussed reasons. This makes comparing various bremsstrahlung results difficult.

4.2 Photoneutron Dose Equivalent Rates

The bremsstrahlung power and the corresponding photoneutron dose equivalent rates, measured 80 cm lateral from the targets, are given in Tables 5 and 6 as a function of beam current. The dose equivalent rate (DE) has been obtained from the net Andersson-Braun count rate N_n using the calibration factors determined earlier. Also given are the corresponding normalized DE values. The errors shown in DE and normalized DE are statistical. Only the BF_3 detector was used during the first run at 11-ID, while both the BF_3 as well as ^{3}He tubes were available for the run at 6-ID. The variation of the neutron dose equivalent rate from each target as a function of the bremsstrahlung power is shown in Figure 8 for the data given in both Tables 5 and 6. The bremsstrahlung power plotted on the x-axis is an accurately measured quantity that relates to the actual storage ring

Table 5: Photoneutron dose equivalent rates at 80 cm lateral from target centers in beamline 11-ID.

Target Material	Beam Current I_b (mA)	Measured Vacuum P (nT)	Bremsstrahlung Power (kW)	Net AB Count Rate N_n (cps)	Neutron Dose Equivalent Rate DE (μrem/h)	Normalized Neutron Dose Equivalent Rate DE (μrem/h/kW)
Fe	96.6	9.26	1.66×10^{-8}	0.081	37.5±3.2	$(2.26\pm0.19)\times10^9$
Fe	93.3	8.95	1.72×10^{-8}	0.091	41.8±6.8	$(2.43\pm0.39)\times10^9$
Fe	90.2	8.70	1.63×10^{-8}	0.070	32.1±6.0	$(1.97\pm0.37)\times10^9$
Fe	81.2	8.04	1.24×10^{-8}	0.070	32.1±6.0	$(2.59\pm0.48)\times10^9$
Fe	80.3	7.96	1.20×10^{-8}	0.057	26.5±5.4	$(2.21\pm0.45)\times10^9$
Fe	72.5	7.23	8.96×10^{-9}	0.045	20.6±4.8	$(2.30\pm0.54)\times10^9$
Cu	96.0	9.20	1.81×10^{-8}	0.116	53.6±7.6	$(2.96\pm0.42)\times10^9$
Cu	93.2	8.92	1.68×10^{-8}	0.091	41.8±6.8	$(2.49\pm0.40)\times10^9$
Cu	87.3	8.51	1.48×10^{-8}	0.094	43.1±6.8	$(2.91\pm0.46)\times10^9$
Cu	83.2	8.12	1.28×10^{-8}	0.091	41.8±6.8	$(3.27\pm0.53)\times10^9$
Cu	77.5	7.71	1.14×10^{-8}	0.060	27.5±5.6	$(2.41\pm0.49)\times10^9$
W	88.3	8.64	1.53×10^{-8}	0.122	56.4±7.8	$(3.68\pm0.51)\times10^9$
W	87.9	8.56	1.58×10^{-8}	0.119	54.8±5.4	$(3.46\pm0.34)\times10^9$
W	79.5	7.82	1.18×10^{-8}	0.082	38.0±6.4	$(3.22\pm0.54)\times10^9$
W	79.2	7.90	1.10×10^{-8}	0.081	37.4±3.2	$(3.40\pm0.29)\times10^9$
W	76.5	7.61	1.07×10^{-8}	0.092	42.4±6.8	$(3.95\pm0.63)\times10^9$
Pb	90.9	8.87	1.62×10^{-8}	0.129	59.5±8.0	$(3.67\pm0.49)\times10^9$
Pb	79.4	7.79	1.20×10^{-8}	0.099	45.7±7.0	$(3.79\pm0.58)\times10^9$
Pb	78.5	7.76	1.12×10^{-8}	0.099	45.7±7.0	$(4.08\pm0.62)\times10^9$
Pb	70.8	7.08	8.96×10^{-9}	0.079	36.2±6.2	$(4.04\pm0.69)\times10^9$

Table 6: Photoneutron dose equivalent rates at 80 cm lateral from target centers in beamline 6-ID.

Target Material and Detector	Beam Current I_b (mA)	Measured Vacuum P (nT)	Bremsstrahlung Power (kW)	Net AB Count Rate N_n (cps)	Neutron Dose Equivalent Rate DE (μrem/h)	Normalized Neutron Dose Equivalent Rate DE (μrem/h/kW)
Fe,BF_3	93.4	9.77	5.31×10^{-9}	0.033	15.4±3.0	$(2.90\pm0.56)\times10^9$
Fe,BF_3	92.7	9.62	5.06×10^{-9}	0.031	14.5±2.8	$(2.87\pm0.55)\times10^9$
Fe,^{3}He	89.1	9.27	4.93×10^{-9}	0.102	12.9±1.4	$(2.61\pm0.28)\times10^9$
Fe,BF_3	78.2	8.41	3.71×10^{-9}	0.026	11.8±2.6	$(3.18\pm0.70)\times10^9$
Cu,^{3}He	90.3	9.44	4.10×10^{-9}	0.081	10.3±1.2	$(2.06\pm0.24)\times10^9$
Cu,BF_3	89.9	9.37	4.88×10^{-9}	0.034	15.7±3.0	$(3.20\pm0.61)\times10^9$
Cu,BF_3	81.1	8.59	4.09×10^{-9}	0.028	13.1±1.8	$(3.21\pm0.44)\times10^9$
Cu,BF_3	62.9	7.02	2.43×10^{-9}	0.018	8.5±2.2	$(3.50\pm0.91)\times10^9$
W,^{3}He	90.0	9.38	5.06×10^{-9}	0.139	17.7±1.6	$(3.49\pm0.32)\times10^9$
W,BF_3	87.0	9.19	4.64×10^{-9}	0.042	19.4±3.2	$(4.17\pm0.69)\times10^9$
W,^{3}He	85.7	9.10	4.63×10^{-9}	0.107	13.5±1.4	$(2.92\pm0.30)\times10^9$
W,BF_3	82.3	8.76	4.19×10^{-9}	0.034	15.5±3.0	$(3.71\pm0.72)\times10^9$
W,^{3}He	77.7	8.30	3.61×10^{-9}	0.111	14.0±1.0	$(3.89\pm0.28)\times10^9$
Pb,BF_3	76.1	8.22	3.55×10^{-9}	0.038	17.7±3.2	$(4.98\pm0.90)\times10^9$
Pb,BF_3	63.9	7.12	2.54×10^{-9}	0.027	12.3±2.6	$(4.84\pm1.02)\times10^9$

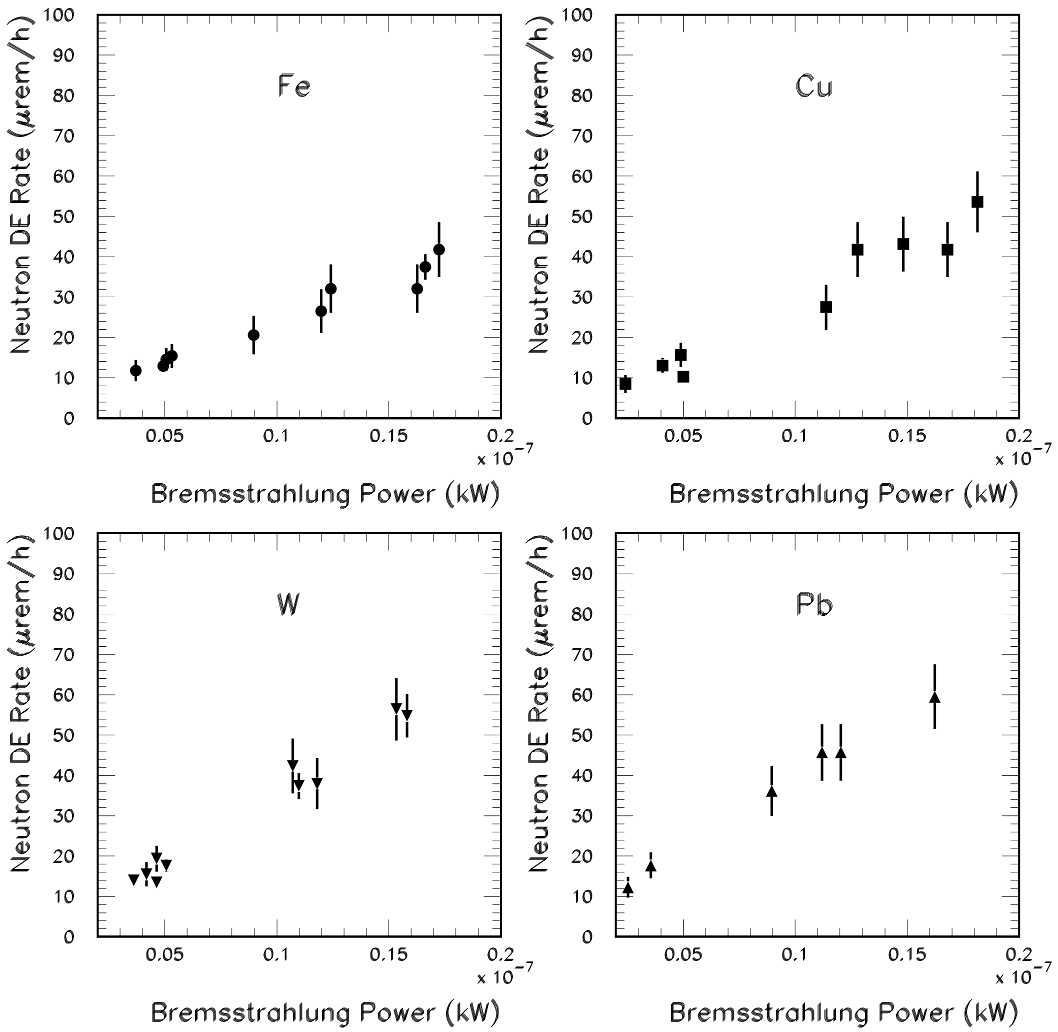

Figure 8: The photoneutron dose equivalent rate, measured 80 cm lateral from each target center, as a function of the incident bremsstrahlung power.

vacuum and beam current variation. Thus, if bremsstrahlung energy or power is known, photoneutron dose equivalent rate from these four target materials can be normalized without having to rely on parameters like the storage ring vacuum and beam current. The variation of the photoneutron dose equivalent rate as a function of the target atomic number Z is not very discernible in Figure 8. Therefore, data in Figure 8 for each target, normalized to the corresponding bremsstrahlung power, are averaged over and plotted as a function of the atomic number Z of the target material as shown in Figure 9 labeled 'present measurements'. The error on the normalized dose rates due to elemental impurities in the targets is insignificant. Photoneutron dose equivalent rates, deduced from previous calculations of the low energy neutron yields released by incident electrons [29], are also shown in Figure 9 for comparison. For W and Pb targets, these values are deduced from calculated neutron yields corresponding to 500 MeV incident electrons - the maximum energy available. Neutron yields up to a maximum energy of 1000 MeV are available for Fe and Cu targets, and has been used for extracting corresponding dose equivalent rates for these targets. Figure 9 shows the present measurements being consistent with the deduced values from previous calculations at high Zs (for W and Pb targets). At low Zs (for Fe and Cu targets), however, results from previous calculations have lower values compared to the present experimental measurements. The present measurements show that the dose equivalent rate increases with the atomic number, though it is not clear whether the variation is linear in nature. Measurements from additional target materials having a Z value between 40 and 60 and also between 10 and 20 are required to fully understand the nature of the curve that would best fit the data in Figure 9.

It is also useful to know the photoneutron dose equivalent rate as a function of stored beam current in case bremsstrahlung energy or power information is not available. However, this will involve uncertainties arising from storage ring vacuum and residual gas variations. The photoneutron dose equivalent contribution as a function of beam current will vary from beamline to beamline because of the bremsstrahlung variation as seen in Figure 6 (B). Thus, using data from Tables 5 and 6, Figure 10 is plotted, which shows the neutron dose equivalent rate, normalized to the estimated storage ring vacuum, from all the four targets as a function of the beam current for beamlines 11-ID

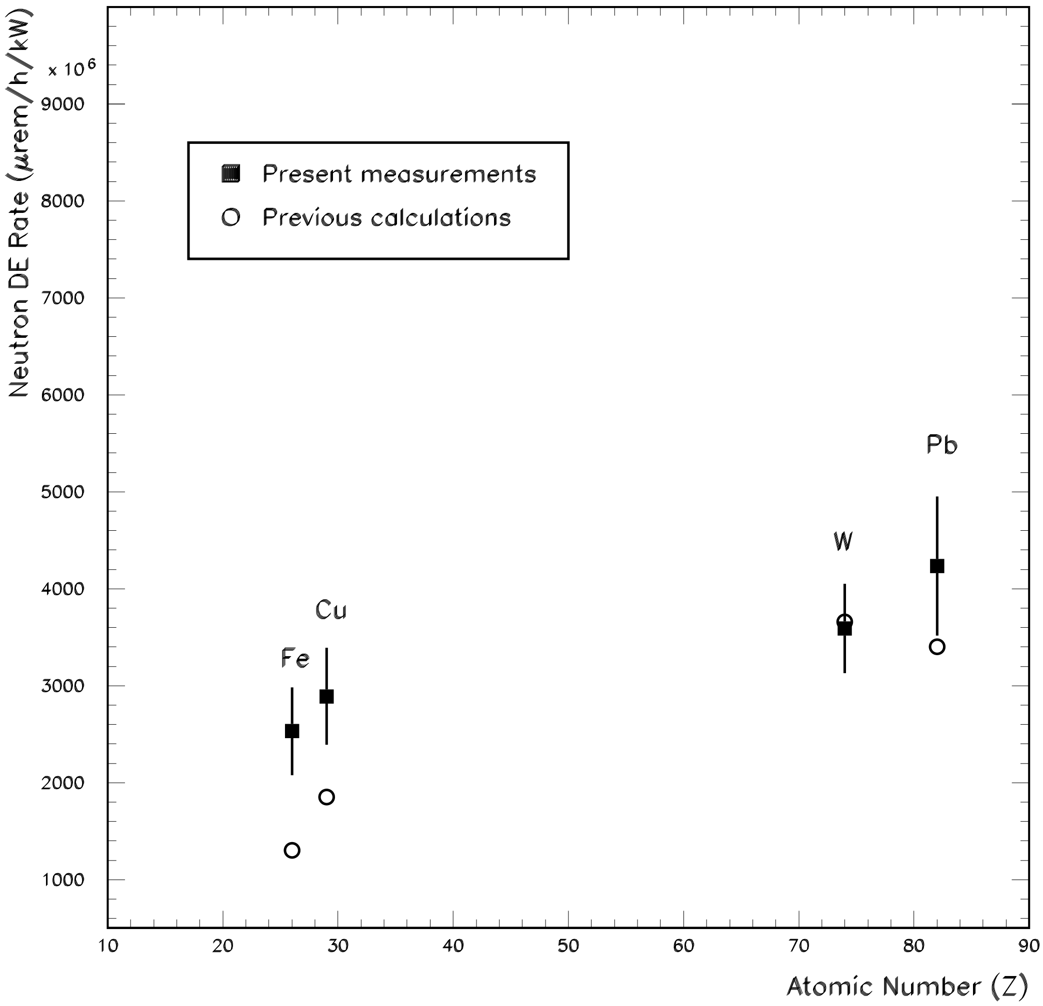

Figure 9: The photoneutron dose equivalent rate at 80 cm perpendicular to each of the target center, normalized to the incident power, shown plotted as a function of the atomic number. The present measurements are the average of all the data from both beamlines 11 ID and 6 ID. The results deduced from previous calculations of photoneutron yields released by incident electrons [29] are also shown for comparison.

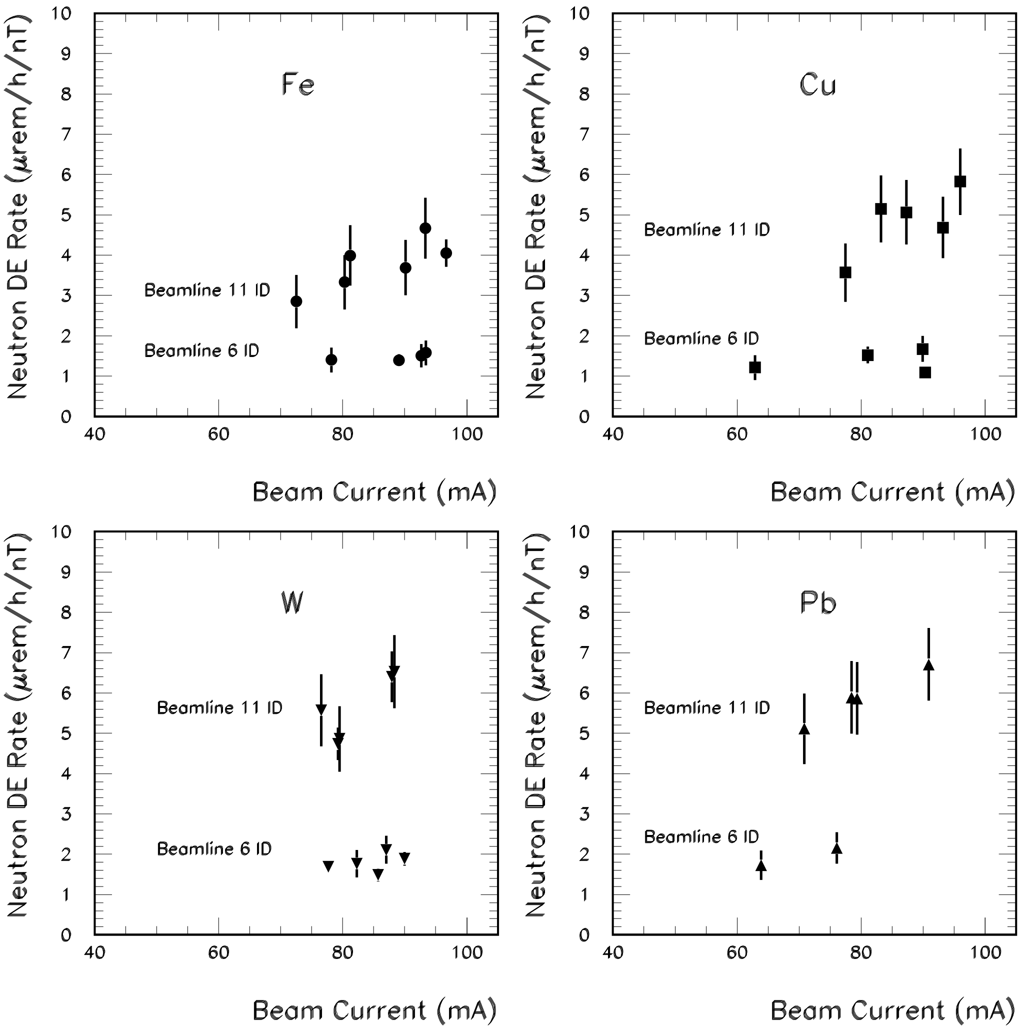

Figure 10: The photoneutron dose equivalent rate at 80 cm lateral from the four targets, normalized to the measured storage ring vacuum, shown plotted as a function of the stored beam current.

and 6-ID. Consistent with the results shown in Figure 6 (B), the vacuum normalized photoneutron dose equivalent rates in Figure 10 vary from beamline to beamline.

To summarize, the average of the bremsstrahlung-normalized photoneutron dose equivalent rates, measured 80 cm perpendicular from the target center in both beamlines, is 2.53±0.45 rem/h/W for Fe, 2.89±0.50 rem/h/W for Cu, 3.59±0.46 rem/h/W for W, and 4.23±0.72 rem/h/W for Pb targets. The average of the beam current and vacuum normalized photoneutron dose equivalent rates, measured 80 cm perpendicular from the target center, is different from beamline to beamline for reasons described earlier in the bremsstrahlung power section. In beamline 11-ID, these are measured as 0.044±0.007 μrem/h/nT/mA for Fe, 0.055±0.009 μrem/h/nT/mA for Cu, 0.068±0.009 μrem/h/nT/mA for W and 0.074±0.011 μrem/h/nT/mA for Pb targets. Similar measurements for beamline 6-ID yielded 0.016± 0.003 μrem/h/nT/mA for Fe, 0.017± 0.003 μrem/h/nT/mA for Cu, 0.021±0.003 μrem/h/nT/mA for W and 0.028±0.005 μrem/h/nT/mA for Pb targets. Systematic corrections that are to be incorporated into these results are discussed in the following section.

4.2.1 Systematic Corrections

The systematic corrections to the measured photoneutron dose equivalent rates should include the thick target correction, correction due to the wall-reflected neutrons (geometrical), and the correction for the non-giant resonance neutron (GRN) dose contribution. The thick target correction addresses the reduction in giant resonance neutron fluence, which the AB remmeter is sensitive to, due to self-absorption within the targets. With our target dimensions, calculations indicate a 6% reduction in the neutron fluence due to self-absorption [38]. The photoneutrons produced could reflect from the concrete ratchet wall close to the target (see Figure 2) resulting in a net artificial increase of actual fluence. The wall reflection of neutrons depends generally upon the photoneutron spectrum and the material of the wall. The AB remmeter response to this artificial fluence increment depends upon it's proximity to the reflecting wall and nature of the reflected neutron spectrum. In the present case, the distance between the concrete wall and the AB remmeter is 121 cm. Calculation estimates a 10% increase in the GRN fluence detected by the AB remmeter due to neutron reflection. An estimation of the correction due to the dose contribution from high energy neutrons (non-GRN) requires the actual high energy photoneutron yield, the corresponding fluence-to-dose conversion factors, and the AB remmeter efficiency at high energies, which is to be folded in in order to determine the response to the dose. An 8% increase in the neutron yield has been estimated from PICA calculations [22] due to high energy neutrons above 20 MeV (non-GRN). Correspondingly, the AB remmeter would have detected an additional 12% GRN dose. The final result of the above discussed corrections is, therefore, an 8% net increase in the measured dose equivalent values.

After applying all the systematic corrections discussed above to the data shown in Table 5 and 6, the average bremsstrahlung-normalized photoneutron dose equivalent rates, 80 cm lateral from the center of the target, are obtained as 2.75±0.49 rem/h/W for Fe, 3.14±0.54 rem/h/W for Cu, 3.90±0.50 rem/h/W for W, and 4.60±0.78 rem/h/W for Pb targets. Likewise, the corrected average of the beam current and vacuum normalized photoneutron dose equivalent rates, measured 80 cm perpendicular from the target center are 0.048±0.008 μrem/h/nT/mA for Fe, 0.060±0.010 μrem/h/nT/mA for Cu, 0.074±0.010 μrem/h/nT/mA for W and 0.080±0.012 μrem/h/nT/mA for Pb targets in beamline 11-ID and 0.017± 0.003 μrem/h/nT/mA for Fe, 0.018± 0.003 μrem/h/nT/mA for Cu, 0.023±0.003 μrem/h/nT/mA for W and 0.030±0.005 μrem/h/nT/mA for Pb targets in beamline 6-ID.

4.2.2 Comparison With Previous Results

Not many measurements of photoneutron dose equivalent rates have been conducted previously at energies as high as that at the APS. Therefore, a true comparison of present results with existing ones is difficult. The existing results from earlier measurements are mostly either from low-energy incident electrons and photons [28, 31] or from using analytical relations and Monte Carlo simulations [29, 30]. The analytical investigations, Monte Carlo calculations and the low-energy incident electron studies have all estimated neutron yields, not the dose equivalent rates, as a function of the incident electron energy or power and the target material and thickness. However, photoneutron dose equivalent rates were deduced from results of a previous calculation of the neutron yields released by low energy incident electrons [29]. The dose equivalent values are extracted from calculated neutron yields at an incident electron energy of 500 MeV for W and Pb targets, and from those at an incident electron energy of 1000 MeV for Fe and Cu targets. These are compared with the present measurements as shown in Figure 9. The agreement is fairly good for W and Pb targets. For Fe and Cu targets, the calculated values are smaller compared to the experimentally measured values. Neutron dose rates, generated from two beamline devices made of copper and tungsten struck by bremsstrahlung produced from a 3 GeV electron storage ring, are discussed by Liu et. al [31]. The results from that study are given normalized to the storage ring vacuum and beam current. A comparison with the results from Liu et. al [31] will be misleading because of the fact that bremsstrahlung power and the corresponding photoneutron dose equivalent rate in the present measurement, normalized to the vacuum and beam current, vary from beamline to beamline for reasons discussed in previous sections. However, an effort has been made to compare with two previous measurements, normalized to the units of μSv/h/A/GeV/μPa/m, for Cu and W targets [31]. These were found to be an order of magnitude higher than the average of all our largest (beamline 11-ID) corresponding measurements for Cu and W targets. Thus, photoneutron dose equivalent rate, normalized to the bremsstrahlung power, is the only quantity to make meaningful comparison with, which are not always available from previous measurements.

Chapter 5

Conclusions

Bremsstrahlung power from insertion device beamlines 11-ID and 6-ID of the APS positron storage ring are accurately measured using a sensitive and fast responding lead-glass electromagnetic calorimeter. The beam current and vacuum normalized bremsstrahlung power is fairly constant within a beamline for a given storage ring fill pattern but may vary from beamline to beamline. They are, on average, measured as 118.0±9 GeV/s/nT/mA from 11-ID and 36±2 GeV/s/nT/mA from 6-ID. These results, along with the results of four previous independent bremsstrahlung measurements [18, 19], enabled us to conclude upon the various reasons causing the variation. The reasons attributed to the difference in the normalized bremsstrahlung power from beamline to beamline are: the variation of vacuum profiles along the vacuum chamber, the variation of residual gas composition in the straight section, the variation of temperature profile along the vacuum chamber due to RF heating, and the presence of a non-gas bremsstrahlung component. The non-gas bremsstrahlung component depends upon the vacuum chamber dimensions, the relative position of the beam halo with respect to the vacuum chamber, and the maximum bunch current in the storage ring as determined by the filling pattern. The bremsstrahlung power, normalized to the storage ring vacuum, is also found to be linear with respect to the beam current. Average normalized bremsstrahlung powers of $(2.0\pm0.14)\times10^{-8}$ W/nT/mA and $(0.6\pm0.03)\times10^{-8}$ W/nT/mA have been measured for beamline 11-ID and 6-ID, respectively.

Using an Andersson-Braun (AB) remmeter with BF_3 and ^3He tubes, simultaneous photoneutron dose equivalent rates are measured as a function of the bremsstrahlung power, from Fe, Cu, W, and Pb thick targets placed in the bremsstrahlung beam at insertion device beamlines 11-ID and 6-ID. The average photoneutron dose equivalent rates, normalized to the bremsstrahlung power, are measured as 2.75±0.49 rem/h/W for Fe, 3.14±0.54 rem/h/W for Cu, 3.90±0.50 rem/h/W for W, and 4.60±0.78 rem/h/W for Pb targets. These results are measured at 80 cm lateral from the center of the target, perpendicular to the photon beam direction. The average of the beam current and vacuum normalized photoneutron dose equivalent rates, measured 80 cm perpendicular from the target center, is different from beamline to beamline because of the difference in the corresponding bremsstrahlung power. In beamline 11-ID, these are measured as 0.048±0.008 μrem/h/nT/mA for Fe, 0.060±0.010 μrem/h/nT/mA for Cu, 0.074±0.010 μrem/h/nT/mA for W and 0.080±0.012 μrem/h/nT/mA for Pb targets. Similar measurements for beamline 6-ID yielded 0.017± 0.003 μrem/h/nT/mA for Fe, 0.018± 0.003 μrem/h/nT/mA for Cu, 0.023±0.003 μrem/h/nT/mA for W and 0.030±0.005 μrem/h/nT/mA for Pb targets.

Future proposed experimental efforts include design and construction of a detector to measure the high energy component of the photoneutron spectrum as well as absolute neutron yield measurements for various target materials using a conventional long counter. Bremsstrahlung dose measurements in tissue equivalent configurations are also being presently conducted.

Bibliography

[1] Levinger, J.S. Theories of Photonuclear Reactions. *Ann. Rev. Nuclear. Sci.* **4**, 13 (1954).

[2] Strauch, K Recent Studies of Photonuclear Reactions. *Ann. Rev. Nuclear. Sci.* **2**, 105 (1952).

[3] Levinger, J.S and Bethe, H.A. Neutron Yield from the Nuclear Photoeffect. *Phys. Rev.* **85**, 577 (1952).

[4] Hayward, E. Photodisintegration of Light Nuclei. *Rev. Mod. Phys.* **35**, 324 (1963).

[5] Mutchler, G.S. The Angular Distributions and Energy Spectra of Photoneutrons from Heavy Elements. *Ph.D. Thesis*, MIT (1966).

[6] Bathow, G., Freytag, E. and Tesch, K. Measurements on 6.3 GeV Electromagnetic Cascades and Cascade-Produced Neutrons. *Nucl. Phys.* **B2**, 669 (1967).

[7] Levinger, J.S. The High Energy Nuclear Photoeffect. *Phys. Rev.* **84**, 43 (1951).

[8] Garvey, J., Patrick, B.H., Rutherglen, J.G. and Smith, I.L. Correlated Neutron-Proton Pairs from the Photodisintegration of Oxygen. *Nucl. Phys.* **70**, 241 (1965).

[9] Roos, C.E. and Peterson, V.Z. Photodissociation of Complex Nuclei at Energies Between the Mesonic Threshold and 1150 MeV. *Phys. Rev.* **124**, 1610 (1961).

[10] Fraenkel, Z. Pion Capture in Complex Nuclei. *Phys. Rev.* **130**, 2407 (1963).

[11] Peterson, V.Z. and Roos, C.E. Production of Photostars by Bremsstrahlung of 250 to 500 MeV. *Phys. Rev.* **105**, 1620 (1957).

[12] Miller, R.D. Photonuclear Stars in Emulsions. *Phys. Rev.* **82**, 260 (1951).

[13] Kikuchi, S. Nuclear Photodissociation by High Energy Synchrotron Gamma-Rays. *Phys. Rev.* **86**, 41 (1952).

[14] Metropolis, N., Bivins, R., Storm, M., Turkevich, A., Miller, J.M. and Friedlander, G. Monte Carlo Calculations on Intranuclear Cascades. I. Low Energy Studies. *Phys. Rev.* **110**, 185 (1958).

[15] Metropolis, N., Bivins, R., Storm, M., Turkevich, A., Miller, J.M. and Friedlander, G. Monte Carlo Calculations on Intranuclear Cascades. II. High-Energy Studies and Pion Processes. *Phys. Rev.* **110**, 204 (1958).

[16] Dostrovsky, I., Rabinowitz, P. and Bivins, R. Monte Carlo Calculations of High-Energy Nuclear Interactions. I. Systematics of Nuclear Evaporation *Phys. Rev.* **111**, 1659 (1958).

[17] Gabriel, T.A. and Alsmiller, R.G. Photonuclear Disintegration at High Energies ($<$ 350 MeV). *Phys. Rev.* **182**, 1035 (1969).

[18] Pisharody, M., Job, P.K., Magill, S., Proudfoot, J. and Stanek, R. Measurement of Gas Bremsstrahlung from the Insertion Device Beamlines of the Advanced Photon Source. Argonne National Laboratory Report, *ANL/APS/LS-260,* Argonne National Laboratory, March 1997

[19] Pisharody, M., Job, P.K., Magill, S., Proudfoot, J. and Stanek, R. Measurement of Gas Bremsstrahlung from Electron Storage Rings. *Nucl. Instr. Methods.* **A401**, 442 (1997).

[20] Berman, B.L. Atlas of Photoneutron Cross Sections. University of California Radiation Laboratory Report, *UCRL 78482*, University of California, 1976.

[21] Dietrich, S.S. and Berman, B.L. Atlas of Photoneutron Cross Sections Obtained with Monoenergetic photons. *Atomic Data and Nuclear Data Tables 38*, 199-338, 1988

[22] Gabriel, T.A. *et al.* PICA, An Intranuclear Cascade Calculation for High Energy Photon-Induced Nuclear Reactions. Oak Ridge National Laboratory Report, *ORNL-4687*, Oak Ridge National Laboratory, 1971.

[23] Bertini, H.W. Low Energy Intranuclear Cascade Calculation. *Phys. Rev.* **131**, 1801 (1963).

[24] Bertini, H.W. Intranuclear Cascade Calculation of Secondary Nucleon Spectra from Nucleon-Nucleus Interactions in the Energy Range 340 to 2900 MeV and Comparisons with Experiment. *Phys. Rev.* **188**, 1711 (1969).

[25] Weisskopf, V.F. Statistics and Nuclear Reactions. *Phys. Rev.* **52**, 295 (1937).

[26] Dresner, L. Oak Ridge National Laboratory Report, *ORNL-CF-61-12-30*, Oak Ridge National Laboratory, 1961 (unpublished).

[27] Gallmeier, F.X. General Purpose Photoneutron Production in MCNP4A. Oak Ridge National Laboratory Report, *ORNL/TM-13073*, Oak Ridge National Laboratory, August 1995.

[28] Barber, W.C. and George, W.D. Neutron Yields from Targets Bombarded by Electrons. *Phys. Rev.* **116**, 1551 (1959).

[29] Swanson, W.P. Improved Calculation of Photoneutron Yields Released by Incident Electrons. *Health Phys.* **37**, 347 (1979).

[30] Mao, X.S., Kase, K.R. and Nelson, W.R. Giant Dipole Resonance Neutron Yields Produced by Electrons as a Function of Target Material and Thickness. *Health Phys.* **70(2)**, 207 (1996).

[31] Liu, J.C., Nelson, W.R. and Kase, K.R. Gas Bremsstrahlung and Associated Photon-Neutron Shielding Calculations for Electron Storage Rings. *Health Phys.*, **68(2)**, 205 (1995).

[32] Nelson, W.R., Hirayama, H. and Rogers, D.W.O. The EGS4 Code System. Stanford Linear Accelerator Center Report, *SLAC-265*, Stanford Linear Accelerator Center, December 1985.

[33] Jones, L.W. and Terwillinger, K.M. Photoneutron Production Excitation Functions to 320 MeV. *Phys. Rev.* **91**, 699 (1953).

[34] Tsai, Y.S. Pair Production and Bremsstrahlung of Charged Leptons. *Rev. Modern Phys.* **46**, 820 (1974).

[35] Liu, J.C., Nelson, W.R., Kase, K.R. and Mao, X.S. Calculations of the Giant-Dipole-Resonance Photoneutrons Using a Coupled EGS4-MORSE Code. *Rad. Prot. Dos.* **70**, 49 (1997).

[36] Emmett, M.B. The MORSE Monte Carlo Radiation Transport Code System. Oak Ridge National Laboratory Report, *ORNL-4972*, Radiation Shielding Information Center, Oak Ridge National Laboratory, 1975.

[37] Andersson, I. and Braun, J. A Neutron Rem Counter. *Nukleonik*, **6**, 237 (1964).

[38] Chapman, G.T. and Storrs, C.L. Effective Neutron Removal Cross Sections for Shielding. Oak Ridge National Laboratory Report, *AECD-3978*, Oak Ridge National Laboratory, 1955.